Geology
February 2023, Volume 51, Issue 4, Pages 402-407
https://doi.org/10.1130/G50785.1
https://archimer.ifremer.fr/doc/00822/93403/

Sea-level fluctuations control the distribution of highly liquefaction-prone layers on volcanic-carbonate slopes

Sultan Nabil [1], Jouet Gwenael [1], Riboulot Vincent [1], Terzariol Marco [1], Garziglia Sebastien [1], Cattaneo Antonio [1], Giraudeau J. [2], Jorry Stephan [1]

[1] Geo-Ocean, UMR6538, Ifremer, CNRS, UBO, UBS, 29280 Plouzané, France
[2] Environnements et Paléoenvironnements Océaniques et Continentaux (EPOC), UMR 5805, Université de Bordeaux, CNRS, 33615 Pessac CEDEX, France

Abstract :

Understanding and quantifying the hazards related to earthquake-induced submarine liquefaction and landslides are particularly significant offshore of tropical volcanic-carbonate islands, where carbonate production competes with volcanism to create highly contrasted lithological successions. To improve the detection of liquefaction-prone layers, we analyzed physical properties and mineralogy and performed 70 dynamic triaxial tests on 25 sediment cores offshore of the eastern side of Mayotte (Comoros archipelago in the western Indian Ocean) in an area that has experienced significant seismicity since 2018. We found that the main parameter controlling the liquefaction potential offshore of Mayotte is the presence of low-density layers with high calcite content accumulating along the slope during lowstands. This phasing with sea-level fluctuations implies a significant recurrent geohazard for tropical volcanic-carbonate islands worldwide. Furthermore, the relationship we found between the cyclic resistance of sediment and its density and magnetic susceptibility represents a time-effective approach for identifying the hazards related to earthquake-induced liquefaction.

INTRODUCTION

Since 2018, the island of Mayotte in the Comoros archipelago (Western Indian Ocean) has faced a seismic crisis related to the birth of an about 820 m high submarine volcano some 50 km offshore the SE coastline (Cesca et al., 2020; Feuillet et al., 2021). As a result of the enhanced seismicity, ground shaking may weaken and destabilize the steep submarine sedimentary slopes (Audru et al., 2006) and potentially generates tsunami waves (Poulain et al., 2022). In this context, understanding and quantifying hazards related to earthquake-induced submarine landslides become a significant challenge. The eastern submarine slope of Mayotte would be especially vulnerable to slope failure by liquefaction because of high accumulations of carbonate and volcanic sediments on steep slopes, locally exceeding 35°. Deposition along the Mayotte slope has been modulated by the sediment supply rate, which is a function of the temporal variability of the production, the shutting down of reefal carbonate and volcanoclastic sediments (Zinke et al., 2003), and the local morphology (Counts et al., 2018). In the present work, triaxial tests were carried out to define the liquefaction potential of shallow sedimentary layers (< 27 mbsf). The aim is to identify new sedimentological and geotechnical criteria to define the regional liquefaction hazard mapping.

RESULTS

Offshore Mayotte (North Mozambique channel - Fig. 1A), the seafloor presents alignments of volcanic cones, especially east of Petite Terre Island where they form a 50 km long ridge down to about 3500 mbsl (Fig. 1A) (Tzevahirtzian et al., 2021). In the North-East study area, failure scars of about 200 m in width affect the upper slope (< 1000 mbsl) while headscarps of about 700 m long run along the flanks of erosive channels in deeper waters (Fig. 1C). In the Pamandzi study area, mass wasting left even larger failure scars near the toe of the

slope, in between 1200 and 1400 mbsl (Fig. 1D). Staircase geometries reminiscent of retrogressive failure are common in most of these scars. During the MAYOBS 19 cruise (Rinnert et al., 2021), twenty-five Calypso piston cores (CS) were collected to characterize the mineralogical, physical, and mechanical properties of the sediments (Fig. 1B).

γ-density and magnetic susceptibility

Piston cores range between 2.25 and 26.28 m long (Table S2). They were analyzed using a Multi Sensor Core Logger (MSCL) to acquire bulk density (γ-density) and volume specific magnetic susceptibility (MS) data. The MS and γ-density profiles obtained on the longest core CS25 (Fig. S1) illustrate the cyclic variability in lithological composition. For this study, γ and MS values were normalized with respect to the maximum and minimum values as follows:

$$\gamma_N = (\gamma - \gamma_{min})/(\gamma_{max} - \gamma_{min}) \quad (1)$$

$$MS_N = (MS - MS_{min})/(MS_{max} - MS_{min}) \quad (2)$$

where the min and max values of γ (1.45 and 1.83 g/cm^3) and MS (2 and 782 SI) are obtained from the 70 tested samples (Table S2).

Dynamic triaxial tests

Dynamic triaxial tests were carried out on samples recovered from different lithological layers (Fig. 1). Each sample was first saturated and consolidated isotropically to a mean effective stress (p_0') equivalent to (or slightly exceeding) the in-situ effective stress (Table S2). Samples were then cyclically sheared by applying a sinusoidal differential stress ($q = \sigma_1 - \sigma_3$). Cyclic test results mainly include (Fig. S2): the cyclic resistance ratio ($CRR = q/(2p_0')$); the normalized mean effective stress (p'/p_0'); the shear strain (ε_s) and the normalized excess pore pressure ($R_u = \Delta u/\sigma_3'$). In this work, two different liquefaction criteria are considered: number of cycles N equal N_{Ru} (when R_u=1) or N_{DA} (number of cycles to reach a double amplitude shear strain of

6% (Olson et al., 2020)). Sixty-three tests were successful (Table S2). Fifty-eight samples liquefied under mean CRR values ranging between 0.13 and 0.69 and *N* values between 3 and 100 (Table S2).

Clay content and mineralogy

The apparent correlation between γ-density and MS of the analysed sediment samples (Fig. 2A) led us to investigate their bulk mineralogical composition from X-ray diffraction (XRD) analyses performed with a Bruker AXS diffractometer (Fig. 2B). The predominant concentrations of three carbonate types (Aragonite, Mg-Calcite, Calcite) are found in the lower-density sediments, while the presence of mafic minerals (i.e. clinopyroxene, plagioclase feldspar) associated with abundant ferromagnetic particles compose the high-MS sediments. The mineralogical composition allows us to determine two end-members: the carbonate-dominated and the volcanic-dominated sediments. The grain size distributions obtained with a Malvern Mastersizer 3000 indicate that carbonate sediments are slightly coarser-grained (Fig. 2C). The amount of clay (< 2 μm) is almost constant. Individual particles in representative sieved (> 63 μm) samples from the 2 end-members were imaged using a scanning electron microscope (SEM, Thermofisher Quanta 200, sputter coated with Au; Fig. 2D). Magnetic particles were separated manually with a magnet. Carbonate-dominated samples show an expected biogenic prevalence (e.g. foraminifera, mollusk shells, echinoids), while volcanic-dominated layers show a biogenic-based matrix with magnetic particles. Insert in Fig. 2D shows a typical magnetic inclusion of regular shape (euhedral, tetrahedral, or octahedral) with rounded edges.

DISCUSSION

Sediment source and physical properties

Slope sedimentation offshore Mayotte comprises carbonate particles produced by the barrier reef and volcanoclastic particles derived from continental erosion and soil denudation of exposed volcanos. The physical parameters (γ-density and MS) and mineralogical composition of the sediments reflect this partitioning between carbonate-dominated and volcanic-dominated end-members (Fig. 2). The highest values in MS prevail in sediments rich in detrital and volcanic minerals (Ellwood et al., 2006) such as feldspar, plagioclase, pyroxene, and zeolites (Hunt et al., 1995). On the other hand, carbonate minerals such as calcite and magnesium-carbonate are diamagnetic and present low MS values (Ellwood et al., 2000). Furthermore, the presence of carbonate-rich deposits is associated with cyclic variations of γ-density along cores (CS25 in Fig. S1D). These γ-density fluctuations are mainly linked to the carbonate mineralogy induced by sea-level changes (Fig. S1A and B): aragonite (specific gravity of 2.93) and high-magnesium calcite (HMC) are mainly produced by neritic carbonates (Boardman, 1978) during highstands (when the Mayotte barrier reef is flooded), while low-magnesium calcite (LMC, specific gravity of 2.7) preferentially accumulates along the slope during lowstands and is mainly of planktic origin (Counts et al., 2019; Paul et al., 2012).

Liquefaction in carbonate-rich sediments

Results of cyclic tests outline the variation of *CRR* as a function of the number of cycles to liquefaction (N_{Ru}) (Fig. 3A). The large variability of *CRR* with MS_N for a given N_{Ru} reveals the distinct cyclic response of sediments. By considering a sub-data set with constant N_{Ru} and γ_N, *CRR* varies linearly with MS_N with a slope of 0.31. When a sub-data set with constant N_{Ru} and MS_N is considered, the *CRR* varies linearly with γ_N with a slope of 0.25. Finally, following (Idriss and Boulanger, 2006), *CRR* was related to *N* by a power relationship of the following form:

$$CRR = (0.25\,\gamma_N + 0.31\,MS_N + 0.39)\,N^{-0.13} \quad (3)$$

The error between observed and calculated *CRR* using equation 3 is shown in Fig. 3B and C. It is distributed normally with a standard deviation σ_d of 0.2. Absolute errors higher than 0.15 occur when N values are consistently higher than 15 (dark gray in Fig. 3B) which corresponds to earthquakes of magnitudes (>7) exceeding those measured in Mayotte (Bertil et al., 2021). This good relationship between *CRR* and *N* showing a strong dependence on γ_N and MS_N clearly illustrates the major role of sediment composition. Thus, based on this data set, assessment of the liquefaction potential given an earthquake can be simplified by determining the MS and the γ-density of the sediment.

The factor of safety and probability of liquefaction

The key assumption of the used method lies on the hypothesis that an earthquake of a given magnitude and site-source distance can be simulated in the laboratory by a number of uniform stress cycles (Liu et al., 2001; Seed and Idriss, 1971). This provides a convenient mean for comparing the *CRR* to the earthquake-induced cyclic stress ratio (*CSR*) (Seed and Idriss, 1971; Whitman, 1971). The *CSR* is estimated by using a simplified equation (equations S1 to S5) considering the peak ground acceleration (Roullé et al., 2022). The factor of safety against liquefaction can then be calculated as follows:

$$FoS = CRR/CSR \quad (4)$$

Fig. 3D illustrates the determination of the *FoS* for core CS25 (additional results in Figs. S3 to S5). The *CRR* values are determined for 15 cycles (Mw = 6.75 at 25 km distance). Under this scenario, we identified two liquefiable layers where FoS < 1 (between 0.5 and 2.5 and 5.5 and 6.25 mbsf). Furthermore, the few layers characterized by lower FoS than the general trend (noted wz for weak zone in Fig. 3) correspond to sediments deposited during glacial lowstand periods of

reduced reef carbonate activity (Fig. S1). The lower γ-density is associated with a higher accumulation of calcite sourced from the exposed reef platform where aragonite-to-calcite diagenetic transformation occurred.

From the calculated σ_d (=0.2) shown in Fig. 3C, the normal distribution of *FoS* and the probability of liquefaction P_L were derived (equations S6 to S9 and Fig. 3D). For core CS25, the *FoS* and P_L values are calculated for two earthquake scenarios (Mw 6 and Mw 6.75 at 25 km from CS25). Fig. 3D and E illustrate how the presence of high carbonate content produces several wz with a non-negligible liquefaction probability. Data in Fig. 3D and E indicate that three layers at around 16, 21, and 25 mbsf are characterized by a FoS higher than 1 but still rather low in terms of P_L. The P_L values decrease with depth tending to zero at specific depths below the seabed (> 21 mbsf for Mw 6.75 and > 2 mbsf for Mw 6 - Fig. 3E).

The recurrent wz in the stratigraphic record in Fig. 3E is associated with the 100 kyrs glacial-interglacial cyclicity of sea-level fluctuations during the late Quaternary. wz are related to periods of low sea-level when the Mayotte barrier reef was subaerially exposed and the aragonite/HMC input was minimum. Sediments in wz are characterized by lower density due to the preferential LMC deposition.

Probability of liquefaction versus geometric characteristics of observed landslides

Three landslides located between 0.5 and 4 km from core CS24 are shown in Fig. 4A. Based on the four cross sections (a, b, c and d) presented in Fig. 4B the initial seabed geometry was reconstructed (Fig. 4B). Those landslides are characterized by flat failure surfaces parallel to the seabed (Fig. 4B) and low slope angles not exceeding 2°. These features can be ascribed to the development of a failure surface along a weak stratigraphic horizon (Locat et al., 2014). The physical properties and probability of liquefaction for an earthquake of Mw 6.75 point out three

weak layers in terms of liquefaction at 9-10m, 14-15 m, and 16-17 mbsf (grey rectangles in Fig. 4C). The intermediate weak layer is surrounded by two stiff layers and its depth below the seabed fits with the mean depths of the three landslides shown in Fig. 4B. By considering constant sedimentation in the area, it is plausible to ascribe the flat failure surfaces shown in Fig. 4B to the triggering of liquefaction of the layers between 9-10 mbsf and 14-15 mbsf. The presence of a weak layer between two stiff layers is an additional factor promoting liquefaction failure between 14 and 15 mbsf (Fig. 4C). Data presented in Fig. 4 validate the approach here presented by confirming that liquefaction in carbonate-rich sediments is primarily controlled by the presence of low-density LMC-dominated layers formed during lowstands.

Beyond the case of the Mayotte slope – volcanic islands, earthquakes, and liquefaction

Submarine failures and landslides have been observed in many locations worldwide on the flanks of carbonate platforms and contribute to the stratigraphic evolution and major geohazard on the surrounding slopes (Harbitz et al., 2012; Janson et al., 2010; Lehrmann et al., 2020; Mulder et al., 2012; Mulder et al., 2017). Even if the impact of tectonic and volcanic activity on carbonate platform development remains poorly understood, many shallow-water carbonate platforms developed in the tropical realm on active or dormant volcanos throughout the Cenozoic (Courgeon et al., 2017). As a result, coeval carbonate-volcanic sedimentation is commonly reported on seamount slopes and adjacent basins (Counts et al., 2018) while the mixing of sediment fluxes depends on the volcanic activity, relief dismantling, and on environmental conditions that allow reef carbonate fabric production. The alternating deposition of such sediments on very steep slopes may therefore act as a preconditioning factor underlying repeated slope failures offshore carbonate platforms.

In the case of carbonate-rich sedimentation, either on isolated carbonate platforms (Counts et al., 2019; Jorry et al., 2020; Paul et al., 2012) or on mixed carbonate-siliciclastic margins (Droxler and Jorry, 2013; Mallarino et al., 2021), the failure mechanism is mainly linked to the depositional architecture of the carbonate system. Sedimentary systems supplied alternating aragonite/HMC and LMC deposits in phase with the interglacial highstand and glacial lowstand periods during the late Quaternary. Consequently, the liquefiable sediment layers along the Mayotte submarine slope originate from these mineralogical changes. Because of the cyclicity of this climate-related sedimentation, our findings point out that instabilities on carbonate slopes may represent a substantial, recurrent geohazard offshore coral reefs especially in seismic and/or volcanic zones such as the Caribbean (e.g. Northern Nicaragua Rise), the Pacific (e.g. Hawaii) or the Indian Ocean (Indonesia).

ACKNOWLEDGMENTS

The French Oceanographic Cruise MAYOBS19 was funded by the Réseau de Surveillance Volcanologique et Sismologique de Mayotte (REVOSIMA) consortium. We thank the chief scientists (E. Rinnert, E. Lebas, and F. Paquet), the cruise scientific team, captains, and crews for their invaluable support during the MAYOBS19 cruise. Thanks to M. Rovere and J. Gouriou for the core analysis at the Ifremer sediment analysis laboratory (Brest, France); S. Cheron and A. Boissier at Ifremer for XRD-XRF measurements; and N. Gayet for help with SEM images. We also thank Simon George, two anonymous reviewers, and editor Rob Strachan for their constructive comments.

REFERENCES CITED

Audru, J.-C., Guennoc, P., Thinon, I., and Abellard, O., 2006, BATHYMAY: Underwater structure of Mayotte Island revealed by multibeam bathymetry: Comptes Rendus Geoscience, v. 338, no. 16, p. 1240-1249.

Bertil, D., Mercury, N., Doubre, C., Lemoine, A., and Van der Woerd, J., 2021, The unexpected Mayotte 2018–2020 seismic sequence: a reappraisal of the regional seismicity of the Comoros: Comptes Rendus. Géoscience, v. 353, no. S1, p. 1-25.

Boardman, M. R., 1978, Holocene deposition in Northwest Providence Channel, Bahamas: a geochemical approach: North Carolina Univ., Chapel Hill (USA).

Cesca, S., Letort, J., Razafindrakoto, H. N. T., Heimann, S., Rivalta, E., Isken, M. P., Nikkhoo, M., Passarelli, L., Petersen, G. M., and Cotton, F., 2020, Drainage of a deep magma reservoir near Mayotte inferred from seismicity and deformation: Nature geoscience, v. 13, no. 1, p. 87-93.

Counts, J. W., Jorry, S. J., Leroux, E., Miramontes, E., and Jouet, G., 2018, Sedimentation adjacent to atolls and volcano-cored carbonate platforms in the Mozambique Channel (SW Indian Ocean): Marine Geology, v. 404, p. 41-59.

Counts, J. W., Jorry, S. J., Vazquez Riveiros, N., Jouet, G., Giraudeau, J., Chéron, S., Boissier, A., and Miramontes, E., 2019, A Late Quaternary record of highstand shedding from an isolated carbonate platform (Juan de Nova, southern Indian Ocean): The Depositional Record, v. 5, no. 3, p. 540-557.

Courgeon, S., Jorry, S. J., Jouet, G., Camoin, G., BouDagher-Fadel, M. K., Bachèlery, P., Caline, B., Boichard, R., Révillon, S., and Thomas, Y., 2017, Impact of tectonic and volcanism on the Neogene evolution of isolated carbonate platforms (SW Indian Ocean): Sedimentary Geology, v. 355, p. 114-131.

Droxler, A. W., and Jorry, S. J., 2013, Deglacial origin of barrier reefs along low-latitude mixed siliciclastic and carbonate continental shelf edges: Annual review of marine science, v. 5, p. 165-190.

Ellwood, B. B., Balsam, W. L., and Roberts, H. H., 2006, Gulf of Mexico sediment sources and sediment transport trends from magnetic susceptibility measurements of surface samples: Marine Geology, v. 230, no. 3-4, p. 237-248.

Ellwood, B. B., Crick, R. E., Hassani, A. E., Benoist, S. L., and Young, R. H., 2000, Magnetosusceptibility event and cyclostratigraphy method applied to marine rocks: detrital input versus carbonate productivity: Geology, v. 28, no. 12, p. 1135-1138.

Feuillet, N., Jorry, S., Crawford, W. C., Deplus, C., Thinon, I., Jacques, E., Saurel, J. M., Lemoine, A., Paquet, F., and Satriano, C., 2021, Birth of a large volcanic edifice offshore Mayotte via lithosphere-scale dyke intrusion: Nature Geoscience, v. 14, no. 10, p. 787-795.

Harbitz, C. B., Glimsdal, S., Bazin, S., Zamora, N., Løvholt, F., Bungum, H., Smebye, H., Gauer, P., and Kjekstad, O., 2012, Tsunami hazard in the Caribbean: Regional exposure derived from credible worst case scenarios: Continental Shelf Research, v. 38, p. 1-23.

Hunt, C. P., Moskowitz, B. M., and Banerjee, S. K., Magnetic properties of rock and minerals, *in* Proceedings Rock physics and phase relations: a handbook of physical constants, Washington, D. C, 1995, AGU, p. 189-203.

Idriss, I. M., and Boulanger, R. W., 2006, Semi-empirical procedures for evaluating liquefaction potential during earthquakes: Soil dynamics and earthquake engineering, v. 26, no. 2-4, p. 115-130.

Janson, X., Eberli, G. P., Lomando, A. J., Bonnaffé, F., Morgan, W. A., George, A. D., Harris, P. M., Kupecz, J. A., and Sarg, J. F., 2010, Seismic characterization of large-scale platform-margin collapse along the Zhujiang carbonate platform (Miocene) of the South China

Sea, based on Miocene outcrop analogs from Mut Basin, Turkey, Cenozoic Carbonate Systems of Australasia, Volume 95, SEPM Special Publication, p. 73-92.
Jorry, S. J., Jouet, G., Edinger, E. N., Toucanne, S., Counts, J. W., Miramontes, E., Courgeon, S., Riveiros, N. V., Le Roy, P., and Camoin, G. F., 2020, From platform top to adjacent deep sea: new source-to-sink insights into carbonate sediment production and transfer in the SW Indian Ocean (Glorieuses archipelago): Marine Geology, v. 423, p. 106144.
Lehrmann, D. J., Minzoni, M., Enos, P., Kelleher, C., Stepchinski, L., Li, X., Payne, J. L., and Yu, M., 2020, Giant sector-collapse structures (scalloped margins) of the Yangtze Platform and Great Bank of Guizhou, China: Implications for genesis of collapsed carbonate platform margin systems: Sedimentology, v. 67, no. 6, p. 3167-3198.
Liu, A. H., Stewart, J. P., Abrahamson, N. A., and Moriwaki, Y., 2001, Equivalent number of uniform stress cycles for soil liquefaction analysis: Journal of Geotechnical and Geoenvironmental Engineering, v. 127, no. 12, p. 1017-1026.
Locat, J., Leroueil, S., Locat, A., and Lee, H., 2014, Weak layers: their definition and classification from a geotechnical perspective, Submarine mass movements and their consequences, Springer, p. 3-12.
Mallarino, G., Francis, J. M., Jorry, S. J., Daniell, J. J., Droxler, A. W., Dickens, G. R., Beaufort, L., Bentley, S. J., Opdyke, B. N., and Peterson, L. C., 2021, Timescale dependent sedimentary record during the past 130 kyr from a tropical mixed siliciclastic–carbonate shelf edge and slope: Ashmore Trough (southern Gulf of Papua): Sedimentology, v. 68, no. 6, p. 2606-2648.
Mulder, T., Ducassou, E., Gillet, H., Hanquiez, V., Tournadour, E., Combes, J., Eberli, G. P., Kindler, P., Gonthier, E., and Conesa, G., 2012, Canyon morphology on a modern carbonate slope of the Bahamas: Evidence of regional tectonic tilting: Geology, v. 40, no. 9, p. 771-774.
Mulder, T., Joumes, M., Hanquiez, V., Gillet, H., Reijmer, J. J. G., Tournadour, E., Chabaud, L., Principaud, M., Schnyder, J. S. D., and Borgomano, J., 2017, Carbonate slope morphology revealing sediment transfer from bank-to-slope (Little Bahama Bank, Bahamas): Marine and Petroleum Geology, v. 83, p. 26-34.
Olson, S. M., Mei, X., and Hashash, Y. M. A., 2020, Nonlinear site response analysis with pore-water pressure generation for liquefaction triggering evaluation: Journal of Geotechnical and Geoenvironmental Engineering, v. 146, no. 2, p. 04019128.
Paul, A., Reijmer, J. J. G., Fürstenau, J., Kinkel, H., and Betzler, C., 2012, Relationship between Late Pleistocene sea-level variations, carbonate platform morphology and aragonite production (Maldives, Indian Ocean): Sedimentology, v. 59, no. 5, p. 1640-1658.
Poulain, P., Le Friant, A., Pedreros, R., Mangeney, A., Filippini, A. G., Grandjean, G., Lemoine, A., Fernández-Nieto, E. D., Díaz, M. J. C., and Peruzzetto, M., 2022, Numerical simulation of submarine landslides and generated tsunamis: application to the on-going Mayotte seismo-volcanic crisis: Comptes Rendus. Géoscience, v. 354, no. S2, p. 1-30.
Rinnert, E., Lebas, E., Jorry, S., Feuillet, N., Thinon, I., and Fouquet, Y., 2019, MAYOBS, https://doi.org/10.18142/291.
Rinnert, E., Paquet, F., and Lebas, E., 2021, MAYOBS19 cruise, RV Pourquoi pas ?, https://doi.org/10.17600/18001985.
Roullé, A., Baillet, M., Bertil, D., and Cornou, C., 2022, Site effects observations and mapping on the weathered volcanic formations of Mayotte Island: Comptes Rendus. Géoscience, v. 354, no. S2, p. 1-25.

Seed, H. B., and Idriss, I. M., 1971, Simplified procedure for evaluating soil liquefaction potential: Journal of the Soil Mechanics and Foundations division, v. 97, no. 9, p. 1249-1273.
Tzevahirtzian, A., Zaragosi, S., Bachèlery, P., Biscara, L., and Marchès, E., 2021, Submarine morphology of the Comoros volcanic archipelago: Marine Geology, v. 432, p. 106383.
Whitman, R. V., 1971, Resistance of soil to liquefaction and settlement: Soils and Foundations, v. 11, no. 4, p. 59-68.
Zinke, J., Reijmer, J. J. G., Thomassin, B. A., Dullo, W. C., Grootes, P. M., and Erlenkeuser, H., 2003, Postglacial flooding history of Mayotte lagoon (Comoro archipelago, southwest Indian Ocean): Marine Geology, v. 194, no. 3-4, p. 181-196.

FIGURE CAPTIONS

Figure 1. (A) General bathymetric map of Mayotte. (B) bathymetric map of the eastern slope of Mayotte Island (Rinnert et al., 2019) with cores plotted as small dots. (C) and (D) show a shaded bathymetric view with core locations in the North-East and the Pamandzi areas. The maps in (C) and (D) illustrate the occurrence of submarine failure scars shaping the slopes.

Figure 2. (A) Relationship between γ-density and MS (magnetic susceptibility) of analyzed sediment samples. Two end-members, volcanic- and carbonate-dominated sediments are identified based on their bulk mineralogical compositions determined by (B) X-ray diffraction (XRD) analysis, (C) Mean grain size distribution and (D) SEM images.

Figure 3. (A) Cyclic resistance ratio (CRR) as a function of number of cycles (N_{Ru}). Numbers indicate MS_N values. (B) Absolute error between observed and calculated CRR is < 0.15 for the majority of the data. (C) The error range is distributed normally with a standard deviation σ_d of 0.2. (D) FoS against liquefaction versus depth obtained for CS25. CRR values are calculated for a number of cycles of 15 while earthquake-induced cyclic stress ratios (CSR) are determined for a hypothetical earthquake of magnitude 6.75 at 25 km from the core. The normal distribution of

the FoS is also shown. (E) Probability to liquefaction (P_L) versus depth calculated for two different earthquake scenarios with Mw 6 and Mw 6.75. Different weak zones are pointed out in this graph and they correspond in first order to the low γ-density layers with higher calcite content (LMC) accumulated during glacial lowstand periods (Marine Isotope Stages, MIS identified in blue shadows; see Fig. S1).

Figure 4. (A) A 3D view focusing on three shallow landslides (see Fig. 1 for location) with the positions of 4 cross sections (a, b, c and d). The bathymetric cross sections shown in (B) allowed the determination of the landslides' thicknesses, which are between 8 and 14 m. (C) The physical properties and the probability of liquefaction for an earthquake of Mw 6.75 located 25 km from core CS24 allow identifying three wz in terms of liquefaction at 9-10 m, 14-15 m and 16-17 mbsf (grey rectangles) fitting with the depth of the observed slope failures.

[1]Supplemental Material. Age model and the details of the probability of liquefaction calculations**.** Please visit https://doi.org/10.1130/XXXX to access the supplemental material, and contact editing@geosociety.org with any questions.

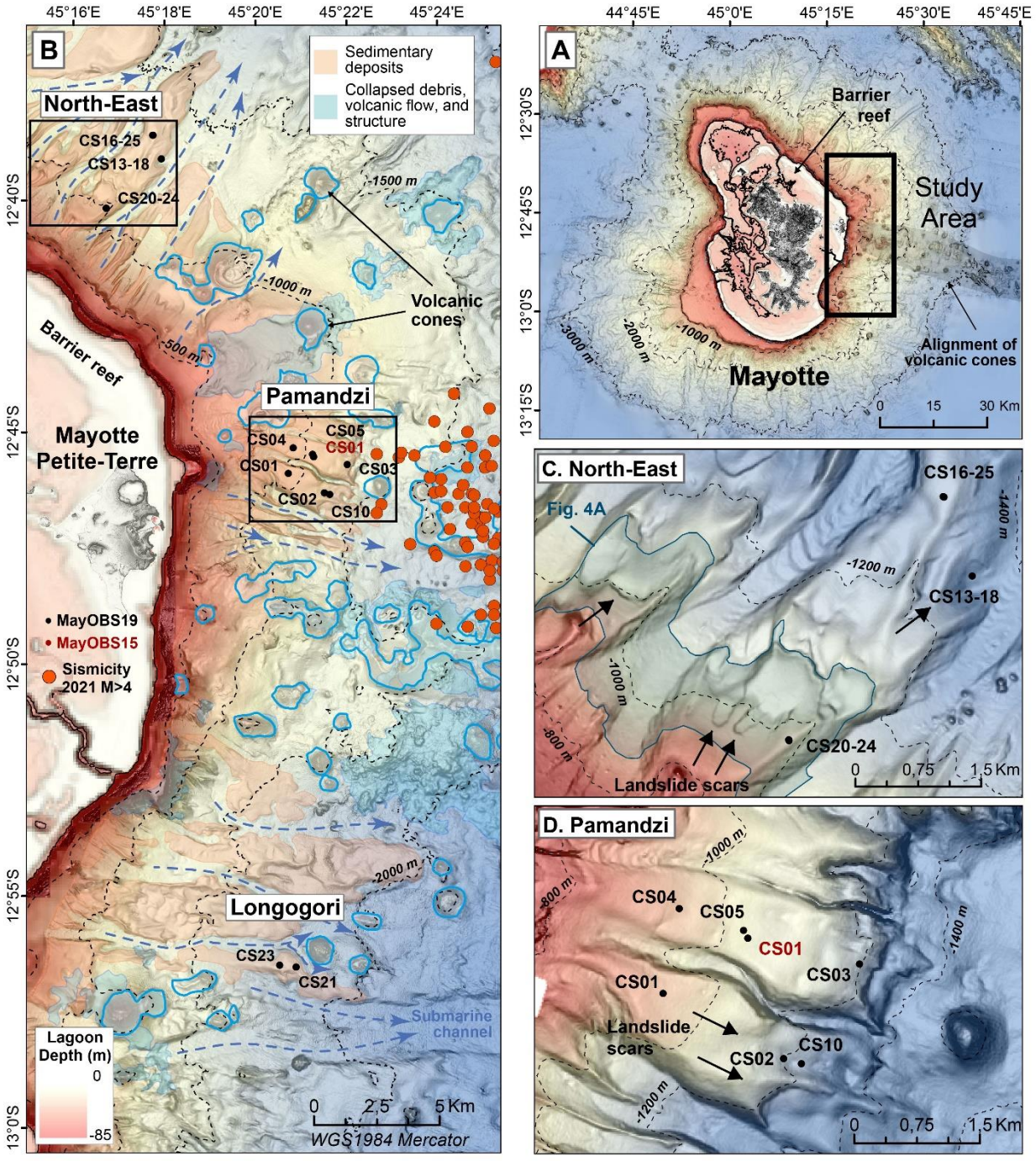
B
North-East
CS16-25
CS13-18
CS20-24
Sedimentary deposits
Collapsed debris, volcanic flow, and structure
-1500 m
-1000 m
-500 m
Volcanic cones
Barrier reef
Pamandzi
CS04
CS05
CS01
CS01
CS03
CS02
CS10
Mayotte Petite-Terre
MayOBS19
MayOBS15
Sismicity 2021 M>4
Longogori
CS23
CS21
-2000 m
Submarine channel
Lagoon Depth (m)
0
-85
0 2,5 5 Km
WGS1984 Mercator
45°16'E
45°18'E
45°20'E
45°22'E
45°24'E
12°40'S
12°45'S
12°50'S
12°55'S
13°0'S
A
Barrier reef
Study Area
Alignment of volcanic cones
Mayotte
-3000 m
-2000 m
-1000 m
0 15 30 Km
44°45'E
45°0'E
45°15'E
45°30'E
45°45'E
12°30'S
12°45'S
13°0'S
13°15'S
C. North-East
Fig. 4A
CS16-25
-1400 m
-1200 m
CS13-18
-1000 m
-800 m
CS20-24
Landslide scars
0 0,75 1,5 Km
D. Pamandzi
-1000 m
-800 m
CS04
CS05
CS01
CS01
CS03
-1400 m
Landslide scars
CS02
CS10
-1200 m
0 0,75 1,5 Km

Figure 1.

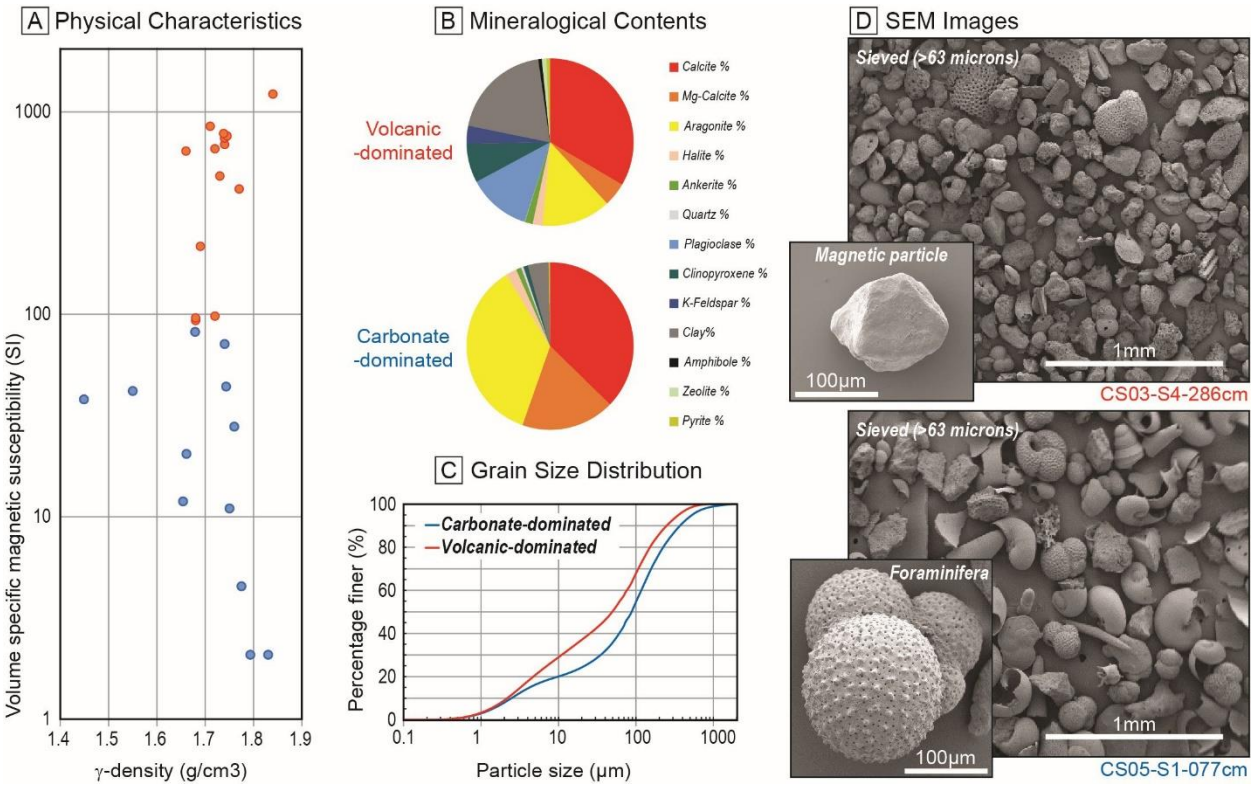
A Physical Characteristics
Volume specific magnetic susceptibility (SI)
γ-density (g/cm3)
B Mineralogical Contents
Volcanic -dominated
Carbonate -dominated
Calcite %
Mg-Calcite %
Aragonite %
Halite %
Ankerite %
Quartz %
Plagioclase %
Clinopyroxene %
K-Feldspar %
Clay%
Amphibole %
Zeolite %
Pyrite %
C Grain Size Distribution
Carbonate-dominated
Volcanic-dominated
Percentage finer (%)
Particle size (μm)
D SEM Images
Sieved (>63 microns)
Magnetic particle
100μm
1mm
CS03-S4-286cm
Sieved (>63 microns)
Foraminifera
100μm
1mm
CS05-S1-077cm

Figure 2.

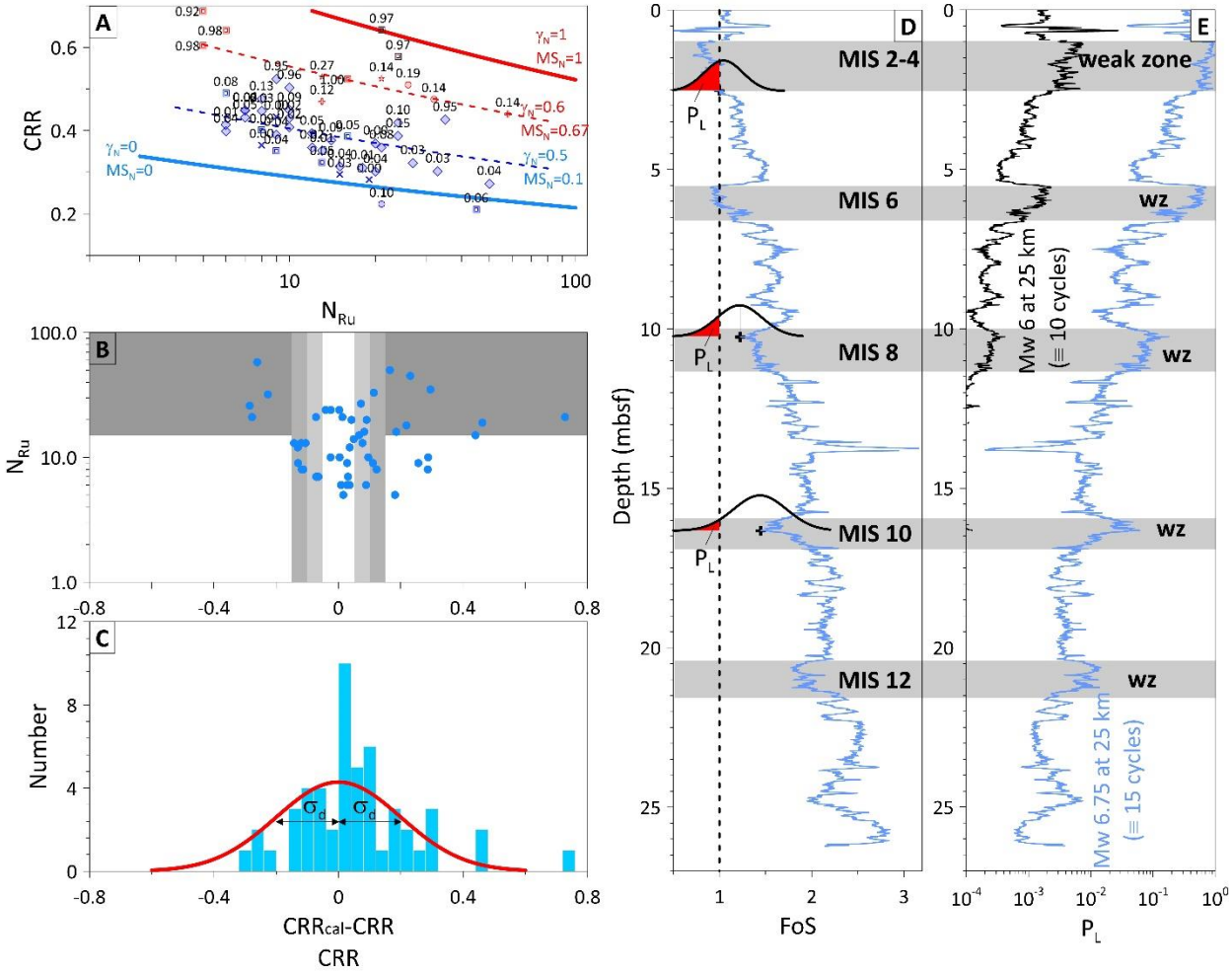
A
B
C
D
E
CRR
N_Ru
γ_N=1
MS_N=1
γ_N=0.6
MS_N=0.67
γ_N=0.5
MS_N=0.1
γ_N=0
MS_N=0
Number
CRRcal-CRR
CRR
σd
Depth (mbsf)
MIS 2-4
MIS 6
MIS 8
MIS 10
MIS 12
P_L
FoS
weak zone
wz
Mw 6 at 25 km
(≡ 10 cycles)
Mw 6.75 at 25 km
(≡ 15 cycles)

Figure 3.

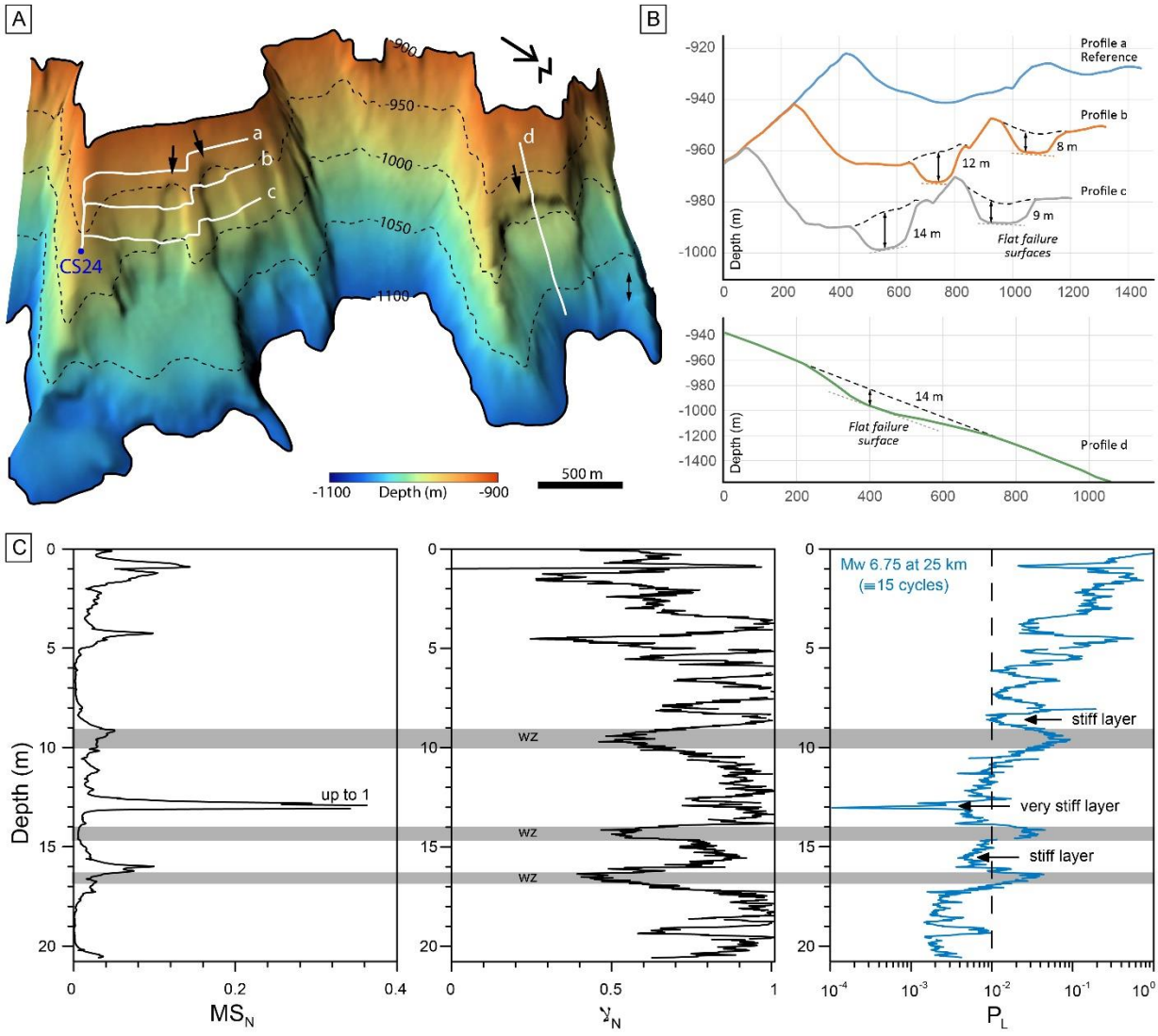
A
B
C
CS24
a
b
c
d
-900
-950
-1000
-1050
-1100
N
-1100
Depth (m)
-900
500 m
Profile a
Reference
Profile b
Profile c
Profile d
12 m
8 m
14 m
9 m
Flat failure
surfaces
Flat failure
surface
Depth (m)
Mw 6.75 at 25 km
(≡15 cycles)
stiff layer
very stiff layer
stiff layer
wz
wz
wz
up to 1
MS_N
ϒ_N
P_L

Figure 4.